Composites Part B 99 (2016) 297–304

Contents lists available at ScienceDirect

Composites Part B

journal homepage: www.elsevier.com/locate/compositesb

Biomediated green synthesis of TiO_2 nanoparticles for lithium ion battery application

Anil A. Kashale [a], Ketan P. Gattu [a], Kalyani Ghule [a], Vijay H. Ingole [a], Swapnali Dhanayat [a], Ramphal Sharma [a], Jia-Yaw Chang [b, **], Anil Vithal Ghule [a, c, *]

[a] Department of Nanotechnology, Dr. Babasaheb Ambedkar Marathwada University, Aurangabad 431004, Maharashtra, India
[b] Department of Chemical Engineering, National Taiwan University of Science and Technology, Taipei 10607, Taiwan
[c] Department of Chemistry, Shivaji University, Kolhapur 416004, Maharashtra, India

ARTICLE INFO

Article history:
Received 8 March 2016
Received in revised form
27 May 2016
Accepted 3 June 2016
Available online 7 June 2016

Keywords:
Nano-structures
Electron microscopy
Biosynthesis
Green
TiO_2
Lithium ion batteries

ABSTRACT

Simple, green and cost effective method is used for the synthesis of TiO_2 nanoparticles, wherein remnant water (ideally kitchen waste) collected from soaked Bengal gram beans (*Cicer arietinum* L.) extract is reacted with $TiCl_4$. Biosynthesized TiO_2 (Bio-TiO_2) nanoparticles with uniform size distribution (free of aggregation even after calcination) were obtained as a result of the stabilizing molecules naturally present in the extract. The morphology, crystal structure and phase composition, specific surface area and pore size distribution of Bio-TiO_2 were systematically investigated by X-ray diffraction (XRD), Raman spectroscopy, transmission electron microscopy (TEM), thermogravimetric analysis (TGA) and BET surface area measurement system. Li-insertion properties were evaluated as anodes in the half-cell configuration (Li/Bio-TiO_2) and it is found to demonstrate reversible insertion of 0.61 mol at a current density of 33 mA g^{-1}. The half-cell displayed a good cyclability and retained 98% of its initial reversible capacity even after 60 galvanostatic cycles.

1. Introduction

Over use of depleting natural resources (coal, oil, natural gas etc.) for circumventing energy demand led to excessive emission of carbon monoxide (CO), carbon dioxide (CO_2) and other green house gases, culminating into global warming issue of great concern. This motivated the drive towards the development of technologies for harvesting energy from renewable energy sources with major focus on solar energy, amongst the other sources like wind, geothermal, hydrothermal etc. These sources of energies though abundant, have their own limitations of storing energy for use when required the most. This concern led to the development of technology for storage devices with major focus on batteries [1,2] and supercapacitors [3–5]. Among the explored storage devices, batteries are considered to be the promising alternative, considering their simplicity, compactness, flexibility to fabricate them, based on the required energy demand in various forms and sizes. Among the batteries, secondary batteries such as nickel-metal hydride batteries (Ni-MH) and lithium ion batteries (LIBs) are proving to be an alternative choice as these serve dual purpose of storing energy generated from nonconventional energy sources and their versatile commercial and industrial applications minimizing pollution, an environmental concern. Thus, extensive work is being done for improving the capabilities of the secondary batteries.

Among all secondary batteries, lithium ion batteries (LIBs) are most promising battery owing to their high power and energy density and longer cycle lifetime. Use of LIBs is not limited to small portable devices, but extends to electric vehicles (EVs) and energy storage systems of wind and solar power energy plants [2,6–8]. However, the key factors affecting the performance of Li-ion batteries consist of anode material. Recent reports show graphitic carbon as commonly used anode material [9,10]. However, the limitations for their practical use in high power batteries include volume expansion and shrinkage during Li-ion intercalation and de-intercalation, which leads to cracking of graphite particles and danger of explosion due to overcharging [11,12]. Thus, developing alternative electrode materials, which would circumvent the limitations, have attracted researchers, particularly for large battery

* Corresponding author. Department of Chemistry, Shivaji University, Kolhapur 416004, Maharashtra, India.
** Corresponding author.
E-mail addresses: jychang@mail.ntust.edu.tw (J.-Y. Chang), anighule@gmail.com (A.V. Ghule).

http://dx.doi.org/10.1016/j.compositesb.2016.06.015
1359-8368/

development. Several materials like CuO [13], Co_3O_4 [14], NiO [15], fiberlike-Fe_2O_3 [16], $Li_{4-x}Ti_5O_{12}$ [17], SnO_2 [18,19], MnO_X [20], Si [21], rutile-TiO_2 [22], anatase-TiO_2 [23] etc. have been explored as an alternative to graphitic carbon. Among these, metal oxides such as CuO, Fe_2O_3, SnO_2, NiO, Si and Co_3O_4 lead to fading capacities due to the high volume expansion and disturbing the structures. This issue is circumvented by making the composites with rGO (Reduced Graphene oxide) and hollow hierarchical metal oxides, wherein the rGO act as a buffer to control the volume changes in above metal oxides [24,25]. However, on the contrary metal oxide such as CeO_2, $Li_4Ti_5O_{12}$ and TiO_2 show relatively less volume expansion during charging/discharging than the above mentioned metal oxides and furthermore their composites are expected to show promising properties.

In the last decade, TiO_2 as an ideal choice amongst the other materials [26], has been extensively studied as an anode material, owing to its easy availability, high abundance, low production cost, non-toxicity, good structural stability, long cycle life, high capacity and very low volume change during lithium ion intercalation/de-intercalation (~4%) [26–29]. Besides, TiO_2 exhibits high lithium ion insertion/desertion voltage (>1.0 V Vs Li^+/Li), which is clearly higher than the operating voltage of graphitic anodes, thus the formation of SEI (Solid Electrolyte Interphase) and electroplating of lithium could be avoided. These characteristics make it a promising anode material for large-scale and long-life energy storage batteries. However, the poor rate capability, poor cycling performance, poor reversibility during first charge-discharge cycle, low ionic and electrical conductivity [30,31] has hampered its use as electrode material in LIBs.

Recently, various attempts have been made to improve the electrical conductivity, diffusion coefficient and address concerns related to irreversibility of Li in electrodes with varying TiO_2 structures. Use of nanomaterials such as nanoparticles [32], nanowires [33] and nanotubes [34] doped with foreign atoms (N, V, Nb, etc.) [35–37], and in combination with highly conductive materials (graphitic like carbon, CNT, etc.) [38,39] have been explored to circumvent the above drawback of anatase TiO_2. Apart from this, aggregation of TiO_2 particles leads to poor rate capabilities due to long diffusion path for Li^+ ions and electrons (e^-) during the lithium ion insertion/extraction process, which leads to poor reversibility [40].

Although, many different synthesis methods (sol-gel [41], electrospinning [42,43], evaporation induced self-assembly (EISA), [44] hydrothermal [45] etc.) have been developed, these processes are complex, energy consuming and difficult to employ for large-scale synthesis [31]. Furthermore, the significance of employing the composite of anatase-rutile phase of TiO_2 is that, improved electrochemical properties are noted with better charge/discharge reversibility when compared to individual phases of TiO_2 [46]. With this motivation, we have attempted a simple, economic and green biosynthesis method to minimize the complexity and make the process cost effective, wherein the composite is formed of the anatase-rutile phase of TiO_2 and carbonaceous material (formed after incomplete oxidation of surface bound and/or trapped biomolecules).

Herein this work, TiO_2 nanoparticles have been biosynthesized (Bio-TiO_2) by completely green approach using remnant water (ideally kitchen waste) collected from soaked Bengal gram beans (*Cicer arietinum* L.). Pectin, a natural bio-molecule present in the extract is found to be responsible for biosynthesis of TiO_2 nanoparticles. Pectin is a complex polysaccharide, that is present in most primary cell walls and it act as bulky complexing reagent. The bulky complex hinders the agglomeration and helps to get the uniform size distribution of particle and thus high surface area of TiO_2 nanoparticles after calcination. This is very helpful to increase the electrical conductivity and diffusion coefficient of Li ion in the structure. Furthermore, characterization of biosynthesized TiO_2 nanoparticles and investigation of electrochemical performance for Li ion battery application is carried out.

2. Experimental section

2.1. Reagents

$TiCl_4$ purchased from Finar was used as such without further purification. Bengal gram beans (*Cicer arietinum* L.) were obtained from local market in Aurangabad, India.

2.2. Synthesis of TiO_2 nanoparticles

The procedure for synthesis of TiO_2 nanoparticles is similar to our previous reports for SnO_2 synthesis [47,48]. In typical process, 20 g of dry Bengal gram beans (*Cicer arietinum* L.) were soaked in 100 mL DI water for 6 h at (25 °C) room temperature. Thereafter, the soaked seeds were removed and the extract was filtrated using a glass-fiber filter (GF/F) to be free from particulate matter. 10 mL of $TiCl_4$ solution was added to 10 mL of the gram bean extract and diluted to 50 mL. The ammonia is added in the diluted solution to make pH of the solution to 7 and formation of titanium-hydroxide-pectin gel, which shrinks and inhibits the further growth of the nanoparticles. The shrinked gel was centrifuged and the powder was air dried and subsequently calcined at 500 °C to remove the organic the contaminants. The TiO_2 nanoparticles (composite of anatase-rutile phase of TiO_2) so produced were characterized for their preliminary structural and morphological properties.

2.3. Electrochemical characterization

Electrochemical studies were carried out in standard two electrode coin-cell (CR 2016) configuration. In electrochemical measurement, metallic lithium was used as both reference and counter electrode. The working/composite electrode was formulated with an accurately weighed 10 mg of active material (Bio-TiO_2), 1.5 mg of conductive additive (super P), and 1.5 mg of teflonized acetylene black (TAB-2) as binder. This composite was then pressed under a pressure of 200 kg cm^{-2} on an area of 200 mm^2 onto a stainless steel mesh, which acts as a current collector. This composite electrode was then subsequently dried at 60 °C for 24 h before assembling the coin-cell under an Ar-filled glove box (MBraun, Germany). The electrodes were separated by a microporous glass fiber separator (Whatman, Cat. No. 1825–047, UK) and filled with 1 M $LiPF_6$ in an ethylene carbonate (EC)/diethyl carbonate (DEC) (1:1 wt%, DAN VEC) mixture as electrolyte.

Cyclic voltammetric (CV) traces were recorded using a Solartron 1470 E potentiostat in a two electrode configuration at a slow scan rate of 0.1 mV s^{-1}. Galvanostatic cycling profiles were recorded using an Arbin 2000 battery tester at a constant current density of 33 mA g^{-1} and for rate capability study by varying current density between 1 and 3 V for half-cell configurations in ambient temperature conditions.

2.4. Material characterization

Powder X-ray diffraction measurement was carried out using Bruker AXS D8 Advance X-ray diffractometer equipped with Cu $K\alpha_1$ radiation between 10° and 80°. Thermogravimetric and differential thermal analysis (TG-DTA) was performed using a TA Instruments SDT-Q600 in the temperature range of 25–900 °C with heating rate of 10 °C min^{-1} in air atmosphere at flow rate of 20 mL min^{-1}. Raman spectrophotometer (STR-150 series, Japan) was used for the

analysis of the samples. Morphology of the as-synthesized Bio-TiO_2 composites and calcined Bio-TiO_2 was observed using transmission electron microscopy (TEM, PHILIPS, CM 200) and selected area electron diffraction (SAED). Specimens were prepared by ultrasonicating Bio-TiO_2 in ethanol followed by dropping the suspension on a carbon-coated copper grid. The surface area and pore volume were determined by nitrogen adsorption/desorption using the Brunauer-Emmett-Teller (BET) method (BET, Micromeretics Tristar 2000, surface area and pore size analyzer). The sample was degassed under inert nitrogen (N_2) at 300 °C for 12 h prior to BET measurements (under standard protocols at 77 K). FTIR spectra were recorded using FTIR (CARRY 600Z series, Japan) to investigate the characteristics functional group of the samples.

3. Results and discussion

Thermal property of the as-prepared Bio-TiO_2 sample (air dried at room temperature) is examined by thermogravimetric analyzer. Fig. 1 shows TG-DTA thermogram of as-prepared Bio-TiO_2 sample. The TGA thermogram shows weight loss of ~25% in the first step in the temperature range from 25 to 110 °C, which accounts to the loss of moisture trapped in the sample [49,50]. The observed high moisture content may be due to the water molecules retained within the surface adsorbed biomolecules and/or absorbed after air drying of the sample. These water molecules are loosely bound and are observed to be lost around 110 °C in TGA thermogram. The weight loss of ~27.3% observed in the temperature range from 110 to 500 °C can be attributed to loss of surface bound organic matter/capping molecules [51] (responsible for preventing aggregation and also maintaining the uniform size distribution of Bio-TiO_2 nanoparticles) transforming into carbonaceous material. Further small decrease in weight (0.99%) in the temperature range from 500 to 900 °C can be attributed to the oxidation of surface bound carbonaceous material as shown in the inset in Fig. 1. This means that the sample contains ~1% of carbonaceous material left in the sample after major decomposition of the biomolecules upto 500 °C.

On the other hand, the DTA thermogram (red curve) shows distinct endothermic peaks at 85 and 245 °C representative of dehydration and decomposition of surface bound organic matter/capping molecules, respectively. Similarly, the small endothermic peaks at 375 and 465 °C can be attributed to the sluggish decomposition of trapped organic matter transforming into carbonaceous material, which were not clearly visible in the TGA curve. In addition to this, a weak endothermic at ~750 °C is also noted corresponding to the oxidation of carbonaceous matter transforming into carbon free TiO_2 nanoparticles.

The structural phase of the sample is investigated by XRD as shown in Fig. 2. The XRD pattern indicates that the TiO_2 powder is composed of mixed anatase and rutile phases belonging to space groups $I4_1/amd$ with Z = 4 and $P4_2/mnm$ with Z = 2, respectively. The phase fraction by weight was determined to be 85.1% of anatase and 14.9% of rutile according to the Rietveld Refinement method implemented in Match-2 software. The XRD pattern of Bio-TiO_2 reveals high crystallinity showing intense peaks at 2θ values of 25.28, 37.81, 48.04, 54.22, 55.16, 62.73, 69.01, 70.18, and 74.97, which could be indexed to (101), (004), (200), (105), (211), (204), (116), (220) and (215) planes of anatase titania [52], respectively (JCPDS 83–2243). On the other hand, the characteristic diffraction peaks at 2θ values of 27.42, 36.11, 41.28, 44.16 and 55.06 could be assigned to (110), (101), (111) and (220) crystal phase of rutile titania [52] (JCPDS 77–0441). The peaks corresponding to the anatase and rutile phases are denoted by "A" and "R", respectively in Fig 2. The XRD pattern is used to calculate the crystallite size for anatase (~13 nm) and rutile phase (~24 nm) using the Scherrer's equation. For pristine Bio-TiO_2 calcined in air for 2 h, the mean crystallite size was determined to be ~14 nm.

Fig. 3 shows N_2 adsorption-desorption isotherm of Bio-TiO_2 recorded to evaluate the surface area. The study reveals that Bio-TiO_2 displays type IV isotherm with a hysteresis loop at the relative pressure P/P_0 ranging from 0.7 to 0.9. The characteristic loop indicates that the Bio-TiO_2 is mesoporous material and the presence of mesopores can be attributed to the decomposition of biomolecules capped on TiO_2 surface and release carbon dioxide during calcination. The BET (Brunauer-Emmett-Teller) surface area calculated from the adsorption isotherm curve is 37.79 $m^2\ g^{-1}$. The inset in Fig. 3 illustrates the corresponding pore size distribution plot calculated by BJH (Barrett-Joyner-Halenda) from the adsorption data. The average pore radius and pore volume of the sample were 4.29 nm and 0.2372 cc g^{-1}, respectively.

Raman spectroscopy is employed for further confirmation of phase of Bio-TiO_2 material as shown in Fig. 4. The Raman spectrum shows characteristic peaks centered at 142 (E_g), 196 (E_g), 397(B_{1g}), 514 (A_{1g}) and 637 cm^{-1} (E_g) revealing anatase phase [53], while the other weak peak located at 446 cm^{-1} (E_g) could be attributed as characteristic of the rutile phase [45]. The intensity of peak clearly indicates that the percentage of anatase phase is more than the rutile phase in Bio-TiO_2.

Room temperature FTIR spectra of drop casted gram bean extract, the as-prepared TiO_2 (air dried) and TiO_2 calcined at 500 °C are shown in Fig. 5. The FTIR spectra of the extract resembles the IR

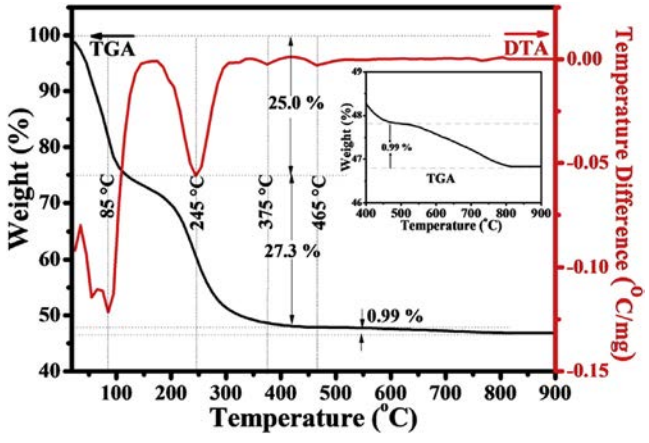

Fig. 1. Representative TG-DTA thermogram of as prepared biosynthesized TiO_2 nanoparticles.

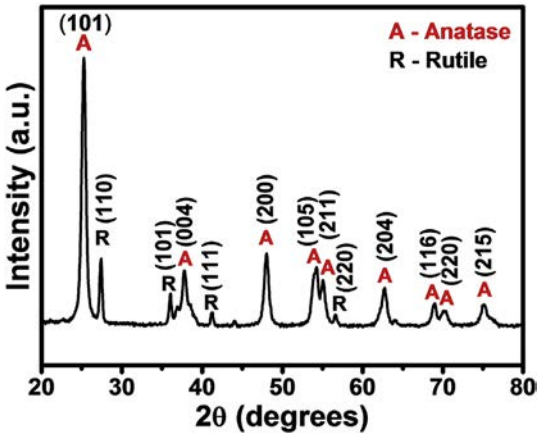

Fig. 2. X-ray diffraction pattern (XRD) of biosynthesized TiO_2 nanoparticles.

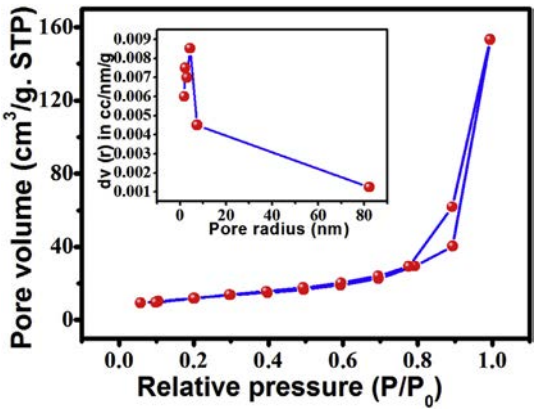

Fig. 3. N_2 adsorption-desorption isotherms and pore radius (nm) distribution (inset) of biosynthesized TiO_2 nanoparticles.

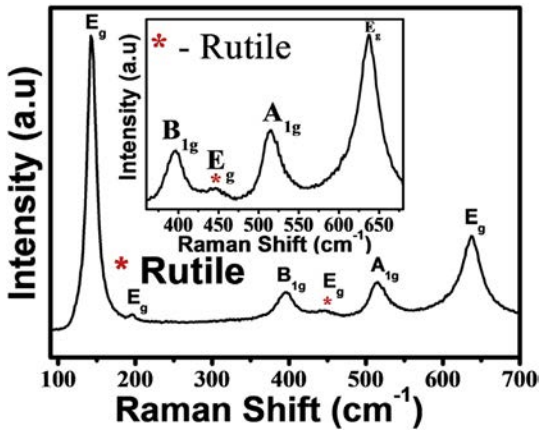

Fig. 4. Representative Raman spectra of biosynthesized TiO_2 nanoparticles.

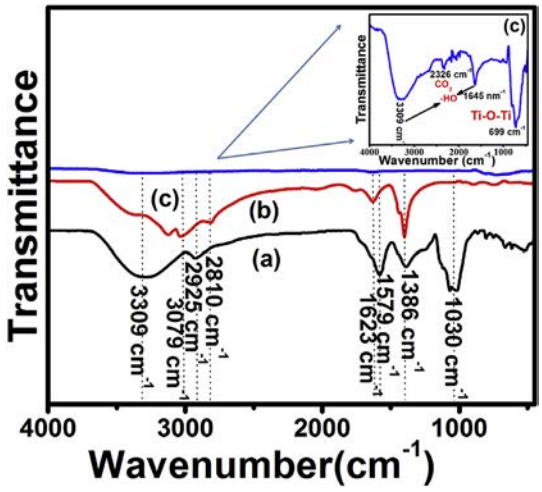

Fig. 5. Representative FTIR of (a) Gram bean extract (b) as prepared biosynthesized TiO_2 (c) Calcined biosynthesized TiO_2.

spectra for pectin revealing its presence in the extract [54]. The obvious intense band (1579 cm^{-1}) in the gram bean extract shows decrease in intensity and shifts ~44 cm^{-1} in as-prepared Bio-TiO_2 due to the stretching mode of the Ti-OOC-R (showing band at 1623 cm^{-1}) [54]. Furthermore, the phenolic −OH group peak at 3309 cm^{-1} shifts to lower wavenumber 3079 cm^{-1} due to the formation of Ti−OH bond. The remaining peaks in pectin−TiO_2 composite induced by pectin were confirmed by comparing of the IR spectrum of the composite with that of the pectin. The peak at 1030 cm^{-1} is assigned to C═O or C═C double bond of pectin. The absorption peaks at 1386 and 1579 cm^{-1} are related to stretching band of COO^- group of pectin [54,55]. It is found that the intensities of peaks around 2925 cm^{-1} (induced by carboxyl and CH_2 groups of pectin) could be attributed to pectin-TiO_2 composite and were obviously weaker than that for pectin. This may originate from the participation of COO^- and CH groups in a hydrogen bond system, which stabilizes the pectin conformation in solid state. The above results indicate that the final product is a true composite of pectin and TiO_2. The pectin peaks were not removed even after washing the sample repeatedly, suggest that the interactions between pectin and TiO_2 are strong. The peak at around 699 cm^{-1}, which refers to Ti−O stretching modes of Ti−*O*−Ti, appeared after calcination at 500 °C. Apart from this, we observed peaks at 1645 and 3309 cm^{-1} which correspond to the surface adsorbed water and hydroxyl groups [56,57]. The peaks at 1044 and 2326 cm^{-1} are related to O−O stretching vibration and carbon dioxide (CO_2), respectively [58].

From the synthesis mechanism summarized in Fig. 6, we can conclude that the autolysis of the cell wall occurs with soaking of gram beans, which results in release of pectin molecules in the extract. These molecules get bound to the titanium ions when titanium chloride is added to the extract [47]. Further, as the pH of the solution is increased up to the 7 by adding ammonia, the titanium-hydroxide-pectin gel shrinks and inhibits the further growth of the nanoparticles. Subsequently, after calcination, we get very small sized nanoparticles with narrow size distribution.

The TEM image of Bio-TiO_2 is shown in Fig. 7a, which depicts aggregation free uniform size distribution of spherical TiO_2 nanoparticles. It is evident from the TEM image that, the biomolecules present in the gram bean extract which act as capping molecules help prevent aggregation of TiO_2 nanoparticles keeping the TiO_2 crystallites apart from each other. These molecules on calcination eventually decompose to form carbonaceous coating, which in turn prevents aggregation. This is in good agreement with TGA study demonstrating oxidation of carbonaceous material (0.99% weight loss) above 500 °C. The particle size of the sample noted from TEM is further confirmed and calculated using Scherrer's equation. Fig. 7b shows particle size distribution histogram with average crystallite size of ~14 nm. The corresponding selected area electron diffraction (SAED) pattern shown in Fig. 7c reveals diffused ring pattern, which is indicative of polycrystalline nature of bio-synthesized TiO_2. It also supports the fact that the resulting TiO_2 consists of mixed phase as confirmed from XRD and Raman study. Furthermore, the SAED pattern clearly indicates the growth of nanoparticles along (101), (004), (200), (110) and (220) planes, which is in agreement with the XRD data.

Electrochemical performance of Bio-TiO_2 was evaluated in half-cell cofiguration (Li/Bio-TiO_2) between 1 and 3 V at room temperature for battery application. Half-cells were subjected to cyclic voltammetric (CV) measurements at scan rate of 0.1 mV s^{-1}, in which metallic lithium acts as counter and reference electrode, respectively. The CV traces of Li/Bio-TiO_2 cell for the first cycle is presented in Fig. 8a. The cell was first discharged to enable insertion of lithium ions into TiO_2 crystal lattice, resulting in a change in valence state of titanium from Ti^{4+} to Ti^{3+}. The CV traces showed sharp peaks at 1.72 and 1.92 V during cathodic and anodic sweeps, respectively. The cathodic scan corresponds to the Li insertion and the anode sweep indicates extraction of the Li ions. Reduction of Ti^{4+} into Ti^{3+} during the cathodic scan and subsequent oxidation of Ti^{3+} to Ti^{4+} during anodic scan indicates the excellent reversibility

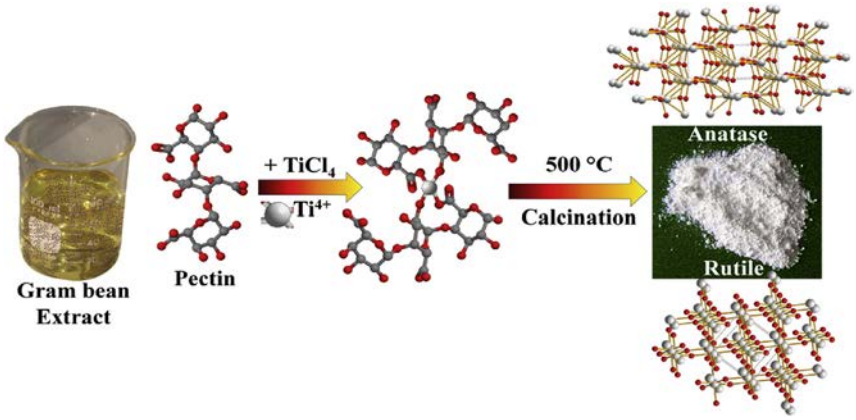

Fig. 6. Schematic representation of biosynthesis mechanism using Gram bean extract Representative TG-DTA thermogram of as prepared biosynthesized TiO_2 powder.

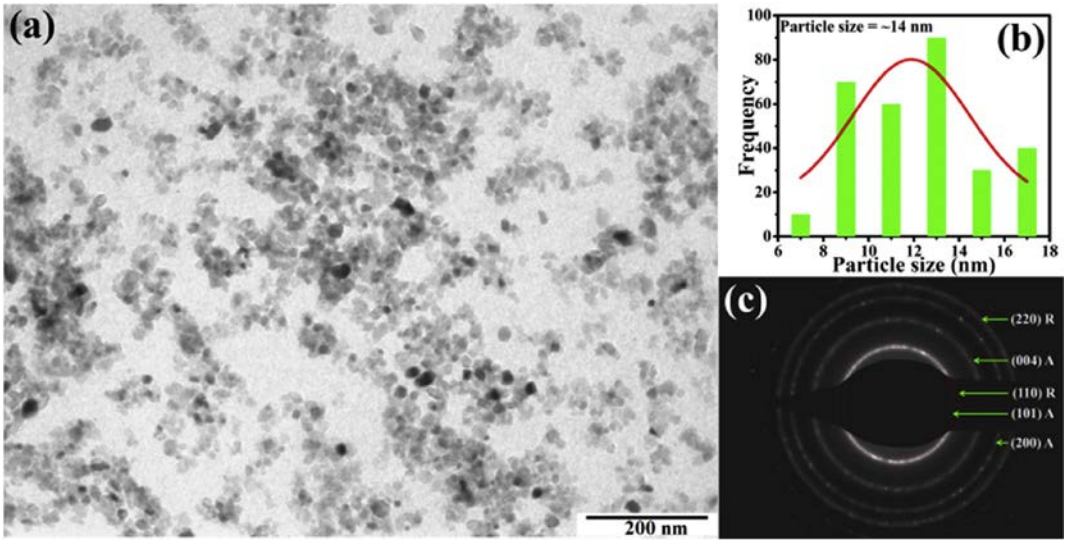

Fig. 7. Representative (a) TEM of biosynthesized TiO_2 nanoparticles. (b) Histogram showing particle size distribution of TiO_2 nanoparticles. (c) SAED pattern of biosynthesized TiO_2 nanoparticles.

of the Bio-TiO_2 insertion host. The sharp oxidation/reduction peaks reveal the two-phase reaction mechanism during electrochemical lithium insertion/extraction according to the following equilibrium: $TiO_2 + xLi^+ + xe^- \leftrightarrow LixTiO_2$ [59].

Galvanostatic cycling stability profiles of Li/Bio-TiO_2 half-cells were performed between 1 and 3 V at a constant current density of 33 mA g^{-1} at room temperature. The typical signature of the charge-discharge curve for first cycle of Li/Bio-TiO_2 cells is shown in Fig. 8b. First, the cell is discharged to intercalate lithium ions into the TiO_2 matrix. During Li intercalation, TiO_2 lattice undergoes a first-order phase transition from tetragonal ($I4_1/amd$) to orthorhombic ($Li_{0.6}TiO_2$, space group $Pnm2_1$) phase, which is due to the loss of symmetry in the y direction [42]. This phase transition occurs along with a spontaneous phase separation of lithium-poor ($Li_{0.01}TiO_2$) into lithium-rich ($Li_{0.69}TiO_2$) phase that has been previously reported by several researchers [60–62]. The cell delivered the initial discharge capacity of 230 mA h g^{-1} at constant current density of 33 mA g^{-1}, and it corresponds to the insertion of 0.69 mol of Li per formula unit. In the first charge cycle, the cell delivered a reversible capacity of 206 mA h g^{-1} (0.61 mol of Li) against the theoretical capacity of 335 mA h g^{-1} for 1 mol of lithium. In the present case, the reversible capacity of 206 mA h g^{-1} is assumed to be 1 C and hence the applied current density 33 mA g^{-1} corresponds to 0.16 C. The irreversible capacity in the first cycle is estimated to be 24 mA h g^{-1}, which corresponds to 0.071 mol of lithium and it is less than some previously reported articles (shown in Table 1). Bio-TiO_2 nanoparticles have uniform size distribution, it is free of aggregation and shows presence of small percentage of carbon (estimated from TG-DTA) which lead to increased surface area and thus increased electrolyte-electrode contact area [63]. The cycling curves show shortened plateau regions or biphase region at ~1.7 and ~1.9 V for discharge (Li insertion) and charge (Li extraction), respectively. This shortened two-phase region co-relates the information that interfacial lithium storage is slightly dominant rather than insertion [64]. The presence of a plateau region during the charge-discharge process is in good agreement with CV traces, and confirms that the Li insertion takes place by a two-phase reaction mechanism.

The cycling profiles of Li/Bio-TiO_2 half-cells tested for 60 cycles between 1 and 3 V at 33 mA g^{-1} constant current density are given in Fig. 8c. It is apparent that the cell delivers more stable cycling profiles with a meagre amount of capacity fading. The cell displayed the discharge capacity of 164 mA h g^{-1} after 60 cycles and 98% columbic efficiency (Fig. 8d) after 60 cycles at a current density of

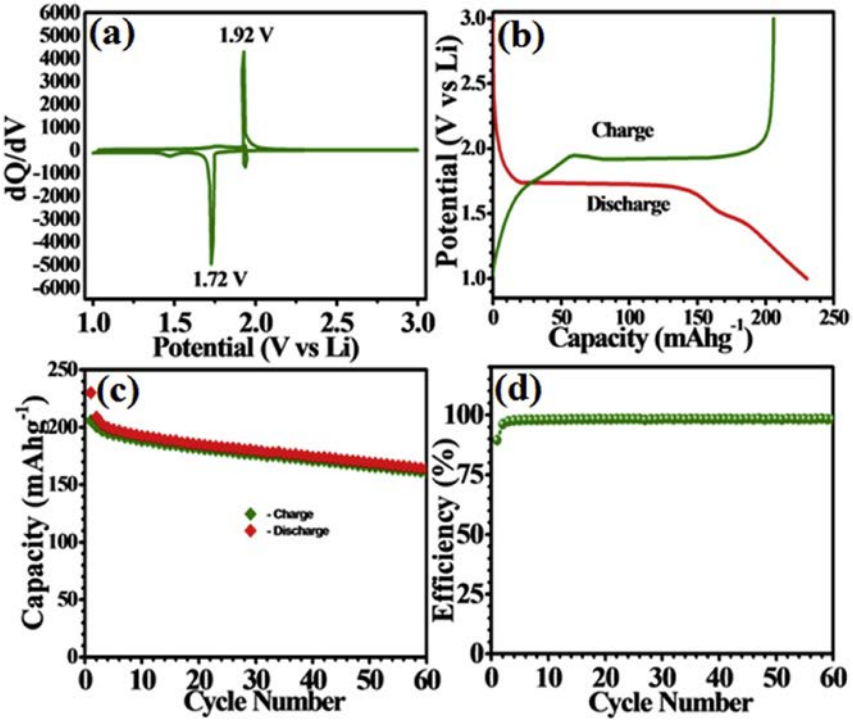

Fig. 8. (a) Cyclic voltammograms (CV) of biosynthesized TiO_2 nanoparticles half-cell cycle between 1 and 3 V at a scan rate of 0.1 mV s^{-1}, in which metallic lithium serves as both counter and reference electrode. (b) Initial charge-discharge curves of Li/TiO_2 half-cell cycle between 1 and 3 V at a current density of 33 mA g^{-1} at room temperature. (c) Cycling stability profiles of the Li/TiO_2 cell and (d) Graph showing Coulombic efficiency (%) vs. number of cycles.

Table 1
Summary of electrochemical performances of representative TiO_2 samples and their composites explored for application in lithium batteries

Compound name	Scan rate (mVs^{-1})	Potential window (V)	Current density	Irreversible capacity during first discharge - charge process (mA h g^{-1})	Capacity at 1st cycle (mA h g^{-1})	Capacity fade after no. of cycles (mA h g^{-1})	Ref.
TiO_2-G Composite Nanofiber	0.1	1–3	33 (mA g^{-1})	~75	~260	~159 (60 Cycles)	[42]
1D-TiO_2 nanofiber	0.1	1–3	33 (mA g^{-1})	~70	~200	~130 (35 Cycles)	[43]
1D-Ag@TiO_2 nanofiber	0.1	1–3	33 (mA g^{-1})	~120	~302	~145 (35 Cycles)	[43]
1D-Au@TiO_2 nanofiber	0.1	1–3	33 (mA g^{-1})	~26	~175	~149 (35 Cycles)	[43]
TiO_2-C	0.1	1–3	33.4 (mA g^{-1})	~12	~195	~105 (10 Cycles)	[44]
TiO_2-C-Cu	0.1	1–3	33.4 (mA g^{-1})	~15	~245	~150 (10 Cycles)	[44]
TiO_2-fiber (Air calcined for 1 h)	–	0.5–3	30 (mA g^{-1})	~23	~220	~178 (10 Cycles)	[66]
P25	0.5	1–3	0.1C	~84	~245	162 (25 Cycles)	[67]
TiO_2(B) (6 M NaOH)	0.5	1–3	0.1C	~11	~240	229 (25 Cycles)	[67]
TiO_2-600	0.1	1–3	0.1C	~20	~230	~185 (100 cycles)	[46]
TiO_2-450	0.1	1–3	0.1C	~7	~180	~160 (100 cycles)	[46]
Bio-TiO_2	**0.1**	**1–3**	**33 (mA g^{-1})**	**24**	**230**	**164 (60 Cycles)**	**This work**

The bold data indicates recent finding in the present work.

33 mA g^{-1}. The capacity fading in the initial cycles is due to the loss of symmetry during phase transition accompanied by a decrease in unit cell along the c-axis. Furthermore, subsequent increase of unit cell volume (~4%) along the b direction results in capacity fading [65]. The Table 1 shows the comparative cyclic performance of Bio-TiO_2 in comparison with earlier reported literature.

Rate capacity study is performed to investigate the versatility and stability of the cell. Fig. 9a shows charge/discharge voltage profiles of Bio-TiO_2 electrode at different current rates. It reveals that the rate capacity strong depends on current density. The discharge capacities of Bio-TiO_2 are about 195, 161, 133, 103, 76, 59 and 46 mA h g^{-1} at various current densities of 33 mA g^{-1}, 125 mA g^{-1}, 250 mA g^{-1}, 500 mA g^{-1}, 1 A g^{-1}, 1.5 A g^{-1} and 2 A g^{-1}, respectively. As shown in Fig. 9b, a specific capacity of ~125 mA h g^{-1} could still be achieved when the current density is switched to 250 mA g^{-1} after 35 cycles (of different current densities) and retained the value for 30 more cycles at 250 mA g^{-1}. The specific capacity (~125 mA h g^{-1}) is comparable to the specific

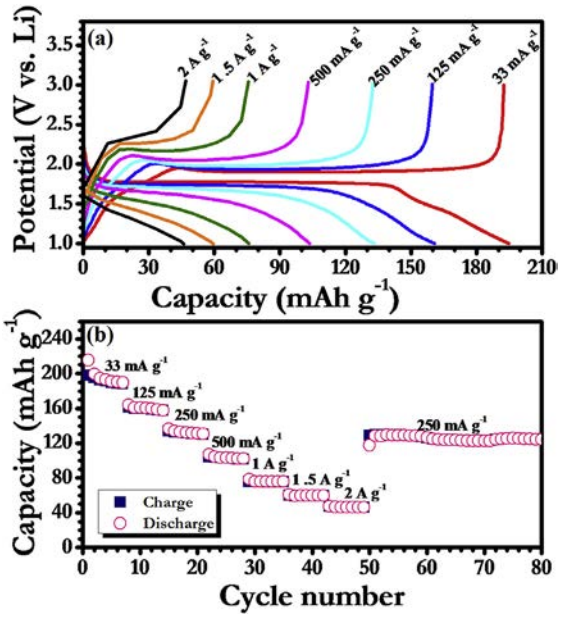

Fig. 9. (a) Galvanostatic discharge/charge voltage profiles at different rates of bio-synthesized Bio-TiO_2 electrode and (b) Rate capability.

capacity in the initial 7 cycles, suggesting excellent rate capability performance and cycle stability of Bi-TiO_2 electrode. This supports the fact that Bio-TiO_2 prepared by bio-mediated green method could be a promising anode material in high power lithium batteries. Furthermore, Bio-TiO_2 with mixed anatase-rutile phase shows comparatively good performance, better charge/discharge reversibility when compared to individual phases of TiO_2 and promising results for its application in Li ion battery and is the subject of interest in the present work. The results discussed herein can be further improved by engineering and modifying the Bio-TiO_2 with other metal dopants, forming composites and by introducing carbonaceous materials coatings over the Bio-TiO_2.

4. Conclusions

In this work, titanium dioxide nanoparticles were successfully biosynthesized using remnant water (ideally kitchen waste) collected from soaked Bengal gram beans (*Cicer arietinum* L.) making it a greener approach. This procedure results in the formation of uniform and non aggregated nanoparticles with narrow size distribution with size ~14 nm, which is confirmed from X-ray diffraction measurement and transmission electron microscopy analysis. The synthesis process is easy, safe, economic and scalable, thus addressing the green chemistry principles. Electrochemical performance of Bio-TiO_2 evaluated in half-cell cofiguration (Li/Bio-TiO_2) between 1 and 3 V in room temperature at current density 33 mA g^{-1} exhibited high reversible capacity of 164 mA g^{-1} after 60 cycles with 98% capacity retention. This performance of the cell is higher than some of the earlier reports summarized as shown in Table 1. The nano-sized Bio-TiO_2 free from aggregation increases the surface area, the electrode/electrolyte contact area, shortens the path lengths for both Li-ion and electron transport and lowers the specific current density, which contributes signficantly in improving the performance and cycling stability of the cell. The synthesis method described in this work is simple, green and economically feasible and thus potentially useful method for producing anodes for high-power Li-ion batteries. This greener method and simple approach can be explored for preparing alternative materials for Li-ion battery and the work in this direction is underway.

Acknowledgements

A. A. K thanks CSIR, New Delhi, for a research fellowship (File no.09/809(0013)/2012-EMR-I). The authors are thankful to UGC-DAE Consortium for Scientific Research, Indore (Project Ref. No: CSR-I/CRS-48/48) and UGC, New Delhi (F. No. 41–370/2012 (SR)) for the financial support. Financial support byMinistry of Science and Technology, R.O.C. Contract No. 102-2628-M-011-001-MY3 is acknowledged.

References

[1] Gören A, Costa CM, Silva MM, Lanceros-Méndez S. State of the art and open questions on cathode preparation based on carbon coated lithium iron phosphate. Compos Part B 2015;83:333–45.
[2] Armand M, Tarascon JM. Building better batteries. Nature 2008;451(7179):652–7.
[3] Li L, Wang S, Hui D, Qiu J. Ordered multiphase polymer nanocomposites for high-performance solid-state supercapacitors. Compos Part B 2015;71:40–4.
[4] Vadiyar MM, Bhise SC, Kolekar SS, Chang J-Y, Ghule KS, Ghule AV. Low cost flexible 3-D aligned and cross-linked efficient ZnFe 2 O 4 nano-flakes electrode on stainless steel mesh for asymmetric supercapacitors. J Mater Chem A 2016;4(9):3504–12.
[5] Wang H, Ma L, Gan M, Zhou T, Sun X, Dai W, et al. Design and assembly of reduced graphene oxide/polyaniline/urchin-like mesoporous TiO_2 spheres ternary composite and its application in supercapacitors. Compos Part B 2016;92:405–12.
[6] Huang S-Z, Cai Y, Jin J, Liu J, Li Y, Yu Y, et al. Hierarchical mesoporous urchin-like Mn_3O_4/carbon microspheres with highly enhanced lithium battery performance by in-situ carbonization of new lamellar manganese alkoxide (Mn-DEG). Nano Energy 2015;12:833–44.
[7] Tompsett DA, Parker SC, Islam MS. Rutile (beta-)MnO_2 surfaces and vacancy formation for high electrochemical and catalytic performance. J Am Chem Soc 2014;136(4):1418–26.
[8] Zhang Z, Wang Y, Tan Q, Zhong Z, Su F. Facile solvothermal synthesis of mesoporous manganese ferrite ($MnFe_2O_4$) microspheres as anode materials for lithium-ion batteries. J Colloid Interface Sci 2013;398:185–92.
[9] Persson K, Sethuraman VA, Hardwick LJ, Hinuma Y, Meng YS, van der Ven A, et al. Lithium diffusion in graphitic carbon. J Phys Chem Lett 2010;1(8):1176–80.
[10] Chung GC, Jun SH, Lee KY, Kim MH. Effect of surface structure on the irreversible capacity of various graphitic carbon electrodes. J Electrochem Soc 1999;146(5):1664–71.
[11] Yazami R. Surface chemistry and lithium storage capability of the graphite-lithium electrode. Electrochim Acta 1999;45(1–2):87–97.
[12] Pupurs A, Varna J. Modeling mechanical stress and exfoliation damage in carbon fiber electrodes subjected to cyclic intercalation/deintercalation of lithium ions. Compos Part B 2014;65:69–79.
[13] Ma X-H, Zeng S-S, Zou B-K, Liang X, Liao J-Y, Chen C-H. Synthesis of different CuO nanostructures by a new catalytic template method as anode materials for lithium-ion batteries. RSC Adv 2015;5(71):57300–8.
[14] Li Y, Tan B, Wu Y. Mesoporous CO_3O_4 nanowire arrays for lithium ion batteries with high capacity and rate capability. Nano Lett 2008;8(1):265–70.
[15] Cheng M-Y, Ye Y-S, Chiu T-M, Pan C-J, Hwang B-J. Size effect of nickel oxide for lithium ion battery anode. J Power Sources 2014;253:27–34.
[16] Liu S, Zhang L, Zhou J, Xiang J, Sun J, Guan J. Fiberlike $Fe_{(2)}O_{(3)}$ macroporous nanomaterials fabricated by calcinating regenerate cellulose composite fibers. Chem Mat 2008;20(11):3623–8.
[17] Borghols WJH, Wagemaker M, Lafont U, Kelder EM, Mulder FM. Size effects in the $Li_{4+x}Ti_5O_{12}$ spinel. J Am Chem Soc 2009;131(49):17786–92.
[18] Kim C, Noh M, Choi M, Cho J, Park B. Critical size of a nano SnO_2 electrode for Li-secondary battery. Chem Mat 2005;17(12):3297–301.
[19] Etacheri V, Seisenbaeva GA, Caruthers J, Daniel G, Nedelec JM, Kessler VG, et al. Ordered network of interconnected SnO_2 nanoparticles for excellent lithium-ion storage. Adv Energy Mater 2015;5(5).
[20] Gu X, Yue J, Li L, Xue H, Yang J, Zhao X. General synthesis of MnOx (MnO_2, Mn_2O_3, Mn_3O_4, MnO) hierarchical microspheres as lithium-ion battery anodes. Electrochim Acta 2015;184:250–6.
[21] Zang J-L, Zhao Y-P. Silicon nanowire reinforced by single-walled carbon nanotube and its applications to anti-pulverization electrode in lithium ion battery. Compos Part B 2012;43(1):76–82.
[22] Yu X-Y, Wu HB, Yu L, Ma F-X, Lou XW. Rutile TiO_2 submicroboxes with superior lithium storage properties. Angew Chem Int Ed 2015;54(13):4001–4.
[23] Weng Z, Guo H, Liu X, Wu S, Yeung KWK, Chu PK. Nanostructured TiO_2 for energy conversion and storage. RSC Adv 2013;3(47):24758–75.
[24] Zhao C, Chou S-L, Wang Y, Zhou C, Liu H-K, Dou S-X. A facile route to synthesize transition metal oxide/reduced graphene oxide composites and their

lithium storage performance. RSC Adv 2013;3(37):16597–603.
[25] Wang B, Wang G, Wang H. Synthesis and electrochemical investigation of hollow hierarchical metal oxide microspheres for high performance lithium-ion batteries. Electrochim Acta 2015;156:1–10.
[26] Kavan L. Lithium insertion into TiO_2 (anatase): electrochemistry, Raman spectroscopy, and isotope labeling. J Solid State Electrochem 2014;18(8):2297–306.
[27] Kang JW, Kim DH, Mathew V, Lim JS, Gim JH, Kimz J. Particle size effect of anatase TiO_2 nanocrystals for lithium-ion batteries. J Electrochem Soc 2011;158(2):A59–62.
[28] Rahman MM, Wang J-Z, Hassan MF, Wexler D, Liu HK. Amorphous carbon coated high grain boundary density dual phase $Li_4Ti_5O_{12}$-TiO_2: a nanocomposite anode material for Li-Ion batteries. Adv Energy Mater 2011;1(2):212–20.
[29] Lin H, Li X, He X, Zhao J. Application of a novel 3D nano-network structure for Ag-modified TiO_2 film electrode with enhanced electrochemical performance. Electrochim Acta 2015;173:242–51.
[30] Xiao L, Cao M, Mei D, Guo Y, Yao L, Qu D, et al. Preparation and electrochemical lithium storage features of TiO_2 hollow spheres. J Power Sources 2013;238:197–202.
[31] Yang M-C, Lee Y-Y, Xu B, Powers K, Meng YS. TiO_2 flakes as anode materials for Li-ion-batteries. J Power Sources 2012;207:166–72.
[32] Rai AK, Anh LT, Gim J, Mathew V, Kang J, Paul BJ, et al. Simple synthesis and particle size effects of TiO_2 nanoparticle anodes for rechargeable lithium ion batteries. Electrochim Acta 2013;90:112–8.
[33] Li J, Wan W, Zhou H, Li J, Xu D. Hydrothermal synthesis of TiO_2(B) nanowires with ultrahigh surface area and their fast charging and discharging properties in Li-ion batteries. Chem Commun 2011;47(12):3439–41.
[34] Ortiz GF, Hanzu I, Djenizian T, Lavela P, Tirado JL, Knauth P. Alternative Li-Ion battery electrode based on self-organized titania nanotubes. Chem Mater 2009;21(1):63–7.
[35] Han H, Song T, Bae J-Y, Nazar LF, Kim H, Paik U. Nitridated TiO_2 hollow nanofibers as an anode material for high power lithium ion batteries. Energy Environ Sci 2011;4(11):4532–6.
[36] Ly Tuan A, Rai AK, Trang Vu T, Gim J, Kim S, Shin E-C, et al. Improving the electrochemical performance of anatase titanium dioxide by vanadium doping as an anode material for lithium-ion batteries. J Power Sources 2013;243:891–8.
[37] Wang Y, Smarsly BM, Djerdj I. Niobium doped TiO_2 with mesoporosity and its application for lithium insertion. Chem Mater 2010;22(24):6624–31.
[38] Ding S, Chen JS, Lou XW. One-dimensional hierarchical structures composed of novel metal oxide nanosheets on a carbon nanotube backbone and their lithium-storage properties. Adv Funct Mater 2011;21(21):4120–5.
[39] Kim M-C, Lee Y-W, Kim S-J, Hwang B-M, Park H-C, Hwang E-T, et al. Improved lithium ion behavior properties of tio2@graphitic-like carbon Core@Shell Nanostructure. Electrochim Acta 2014;147:241–9.
[40] Trang Vu T, Rai AK, Gim J, Kim S, Kim J. Effect of Mo^{6+} doping on electrochemical performance of anatase TiO_2 as a high performance anode material for secondary lithium-ion batteries. J Alloy Compd 2014;598:16–22.
[41] Kubiaka P, Geserick J, Huesing N, Wohfahrt-Mehrens A. Electrochemical performance of mesoporous TiO_2 anatase. J Power Sources 2008;175(1):510–6.
[42] Zhang X, Aravindan V, Madhavi S. Electrospun tio_2-graphene composite nanofibers as a highly durable insertion anode for lithium ion batteries. J Phys Chem C 2012;116(28):14780.
[43] Nam SH, Shim H-S, Kim Y-S, Dar MA, Kim JG, Kim WB. Ag or Au nanoparticle-embedded one-dimensional composite TiO_2 nanofibers prepared via electrospinning for use in lithium-ion batteries. ACS Appl Mater Interface 2010;2(7):2046–52.
[44] Lee SG, Deng H, Hu J, Zhou L, Liu H. Anodic performance of mesoporous TiO_2-C composites with Cu nanopaticles embedded for lithium ion battery. Int J Electrochem Sci 2013;8(2):2204–19.
[45] Shen J, Wang L. Anatase/rutile TiO_2 nanocomposite microspheres with hierarchically porous structures for high-performance lithium-ion batteries. RSC Adv 2012;2(24):9173.
[46] Wei J, Liu J-X, Wu Z-Y, Zhan Z-L, Shi J, Xu K. Research on the electrochemical performance of rutile and anatase composite TiO_2 nanotube arrays in lithium-ion batteries. J Nanosci Nanotechnol 2015;15(7):5013–9.
[47] Gattu KP, Ghule K, Kashale AA, Ghule AV. Bio-green synthesis of Ni-doped tin oxide nanoparticles and its influence on gas sensing properties. RSC Adv 2015;5(89):72849.
[48] Gattu KP, Ghule K, Kashale AA, Ghule AV. Room temperature ammonia gas sensing properties of biosynthesized tin oxide nanoparticle thin films. Curr Nanosci 2015;11(2):253–60.
[49] Peng WM, Wu QY, Tu PG. Pyrolytic characteristics of heterotrophic Chlorella protothecoides for renewable bio-fuel production. J Appl Phycol 2001;13(1):5–12.
[50] Jena J, Pradhan N, Nayak RR, Dash BP, Sukla LB, Panda PK, et al. Microalga scenedesmus sp.: a potential low-cost green machine for silver nanoparticle synthesis. J Microbiol Biotechnol 2014;24(4):522–33.
[51] Faria EHd, Marçal AL, Nassar EJ, Ciuffi KJ, Calefi PS. Sol-Gel TiO_2 thin films sensitized with the mulberry pigment cyanidin. Mat Res 2007;10(4):413–7.
[52] Dong L, Li M, Dong L, Zhao M, Feng J, Han Y, et al. Hydrothermal synthesis of mixed crystal phases TiO_2-reduced graphene oxide nanocomposites with small particle size for lithium ion batteries. Int J Hydrogen Energy 2014;39(28):16116–22.
[53] Ohsaka T, Izumi F, Fujiki Y. Raman spectrum of anatase, TiO_2. J Raman Spectrosc 1978;7(6):321–4.
[54] Shi L, Gunasekaran S. Preparation of pectin-ZnO nanocomposite. Nanoscale Res Lett 2008;3(12):491–5.
[55] Ling C, Liu F, Pei Z, Zhang X, Wei M, Zhang Y, et al. Citric acid enhanced copper removal by a novel multi-amines decorated resin. Sci Rep 2015;5.
[56] Jeong J-H, Jung D-w, Shin EW, Oh E-S. Boron-doped TiO_2 anode materials for high-rate lithium ion batteries. J Alloys Comp 2014;604:226–32.
[57] Feng N, Zheng A, Wang Q, Ren P, Gao X, Liu S-B, et al. Boron environments in B-Doped and (B, N)-Codoped TiO_2 photocatalysts: a combined solid-state nmr and theoretical calculation study. J Phys Chem C 2011;115(6):2709–19.
[58] Mali SS, Betty CA, Bhosale PN, Patil PS. Synthesis, characterization of hydrothermally grown mwcnt-tio_2 photoelectrodes and their visible light absorption properties. ECS J Solid State Sci Technol 2012;1(2):M15–23.
[59] Patoux S, Masquelier C. Lithium insertion into titanium phosphates, silicates, and sulfates. Chem Mater 2002;14(12):5057–68.
[60] Cava RJ, Murphy DW, Zahurak S, Santoro A, Roth RS. The crystal structures of the lithium-inserted metal oxides $Li_{0.5}TiO_2$ anatase, $LiTi_2O_4$ spinel, and $Li_2Ti_2O_4$. J Solid State Chem 1984;53(1):64–75.
[61] Yang Z, Choi D, Kerisit S, Rosso KM, Wang D, Zhang J, et al. Nanostructures and lithium electrochemical reactivity of lithium titanites and titanium oxides: a review. J Power Sources 2009;192(2):588–98.
[62] Wagemaker M, Kentgens APM, Mulder FM. Equilibrium lithium transport between nanocrystalline phases in intercalated TiO_2 anatase. Nature 2002;418(6896):397–9.
[63] Yao H-R, Yin Y-X, Guo Y-G. Size effects in lithium ion batteries. Chin Phys B 2016;25(1).
[64] Shin J-Y, Samuelis D, Maier J. Sustained lithium-storage performance of hierarchical, nanoporous anatase TiO_2 at high rates: emphasis on interfacial storage phenomena. Adv Funct Mater 2011;21(18):3464–72.
[65] Sudant G, Baudrin E, Larcher D, Tarascon JM. Electrochemical lithium reactivity with nanotextured anatase-type TiO_2. J Mater Chem 2005;15(12):1263–9.
[66] Qing R, Liu L, Bohling C, Sigmund W. Conductivity dependence of lithium diffusivity and electrochemical performance for electrospun TiO_2 fibers. J Power Sources 2015;274:667–75.
[67] Wu H-Y, Hon M-H, Kuan C-Y, Leu I-C. Preparation of TiO_2(B) nanosheets by a hydrothermal process and their application as an anode for lithium-ion batteries. J Electron Mater 2014;43(4):1048–54.